Structure and subunit arrangement of *Mycobacterial* F_1F_O ATP synthase and novel features of the unique mycobacterial subunit δ

Neelagandan Kamariah [a], Roland G. Huber [b], Wilson Nartey [a], Shashi Bhushan [a, c], Peter J. Bond [b, d], Gerhard Grüber [a, b, *]

[a] *Nanyang Technological University, School of Biological Sciences, 60 Nanyang Drive, Singapore 637551, Singapore*
[b] *Bioinformatics Institute (BII), Agency for Science, Technology and Research (A*STAR), #07-01 Matrix, 30 Biopolis Street, Singapore 138671, Singapore*
[c] *NTU Institute of Structural Biology, Nanyang Technological University, Singapore*
[d] *Department of Biological Sciences (DBS), National University of Singapore (NUS), 14 Science Drive 4, Singapore 117543, Singapore*

ARTICLE INFO

ABSTRACT

In contrast to other prokaryotes, the *Mycobacterial* F_1F_O ATP synthase (α_3:β_3:γ:δ:ε:a:b:b':c_9) is essential for growth. The mycobacterial enzyme is also unique as a result of its 111 amino acids extended δ subunit, whose gene is fused to the peripheral stalk subunit *b*. Recently, the crystallographic structures of the mycobacterial α_3:β_3:γ:ε-domain and *c* subunit ring were resolved. Here, we report the first purification protocol of the intact *M. smegmatis* F_1F_O ATP synthase including the F_1-domain, the entire membrane-embedded F_O sector, and the stator subunits *b'* and the fused *b*-δ. This enzyme purification enabled the determination of the first projected 2D- and 3D structure of the intact *M. smegmatis* F_1F_O ATP synthase by electron microscopy (EM) and single particle analysis. Expression and purification of the fused mycobacterial *b*-δ_{24-446} construct, excluding the membrane-embedded N-terminal amino acids, provided insight into its secondary structure. By combining these data with homology and *ab-initio* modeling techniques, a model of the mycobacterial peripheral stalk subunits *b*-δ and *b'* was generated. Superposition of the 3D *M. smegmatis* F-ATP synthase EM-structure, the α_3:β_3:γ:ε and *c*-ring, and the derived structural models of the peripheral stalk enabled a clear assignment of all F-ATP synthase subunits, in particular with respect to the unique mycobacterial peripheral stalk subunit *b'* and the elongated δ fused with subunit *b*. The arrangement of δ relative to the N-termini of the catalytic $\alpha_3\beta_3$-headpiece and its potential as a drug target are discussed.

1. Introduction

Tuberculosis (TB) remains one of the leading worldwide causes of infectious disease mortality globally with over one million annual deaths (World Health Organization, 2018), making the bacterium *Mycobacterium tuberculosis*, which mainly causes TB, the most important bacterial pathogen in the world. The *Mycobacterial* F_1F_O ATP synthase (F-ATP synthase), composed of nine subunits with a stoichiometry of α_3:β_3:γ:δ:ε:a:b:b':c_9, has been shown to be essential for growth. This is different from other prokaryotes, where the enzyme is dispensable for growth on fermentable carbon sources and where increased glycolytic flux can compensate for the loss of oxidative phosphorylation (Sassetti et al., 2003; Cook et al., 2014). The enzyme is composed of a membrane-bound F_O section (subunits a:b:b':c_9), and a water-soluble F_1 portion (Fig. 1A). The latter includes subunits $\alpha_3\beta_3$, which form a six-fold pseudo-symmetric ring that sits on top of a central stalk (subunits $\gamma\varepsilon$) (Zhang et al., 2019; Fig. 1A). The bottom of the central stalk sits on a ring of nine *c*-subunits (Preiss et al., 2015), which is proposed to be held against subunit *a* by the so-called peripheral stalk, which itself is composed of the two subunits *b* and *b'*. As in other F-ATP synthases (Sobti et al., 2016; Guo and Rubinstein, 2018; Colina-Tenorio et al., 2018; Hahn et al, 2016), the peripheral stalk is proposed to be attached to the top of the F_1 region by subunit δ (OSCP in mitochondria; Hahn et al, 2016; Srivastava et al. 2018) so that together the central and peripheral stalks establish two connections between the F_1 and F_O regions of the complex (Gajadeera and Weber, 2013; Lu et al., 2014). Movement of protons across the subunits *a-c* generates a proton-motive force that fuels the rotation of the *c*-ring, which interacts with both the

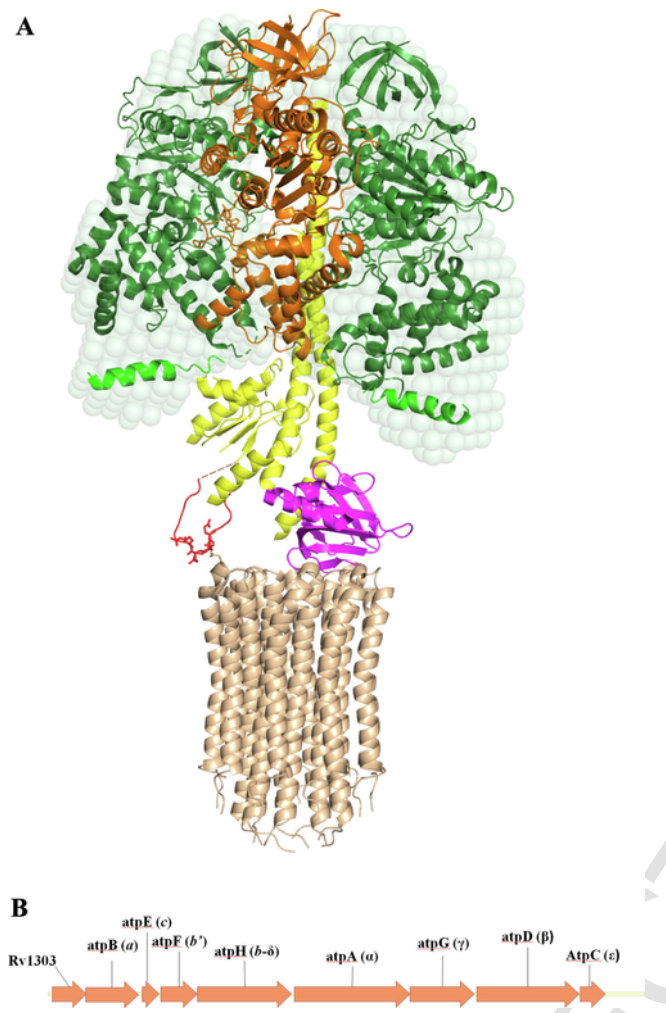**Fig. 1.** (*A*) The structural model of the $\alpha_3\beta_3\gamma\epsilon c$ complex of the mycobacterial F-ATP synthase. Subunits α (*green*), β (*orange*), γ (*yellow*), and ϵ (*magenta*) are from the *M. smegmatis* crystal structure ((PDB ID: 6FOC; Zhang et al., 2018), whereby the missing β-sheet elements of subunit γ were added by the respective subunit γ elements of the *E. coli* F-ATP synthase (PDB ID: 5T4Q; Sobti et al., 2014). Subunit γ has a unique γ-loop (Hotra et al., 2016) in case of the mycobacterial one which is highlighted in *red*. The solution shape of α^{chi} is displayed as *green sphere* (Ragunathan et al., 2017). The *c*-ring loop residues of *M. phlei* (*wheat*; PDB ID: 4V1G; Preiss et al., 2015), proposed to interact with the rotating ϵ and γ stalks subunits are indicated. (*B*) The F-ATP synthase operon of *M. tuberculosis* showing the large size of the *atpH* gene, encoding the *b*-δ fusion protein, and the smaller *atpF* gene for the shorter *b*-type subunit, *b'*. (For interpretation of the references to colour in this figure legend, the reader is referred to the web version of this article.)

N-terminal domain of subunit ϵ and the globular domain of subunit γ to transfer energy to the catalytic α- and β-subunits for ATP synthesis (Capaldi et al. 1996; Noji et al., 1997; Diez et al., 2004; Nakanishi-Matsui et al., 2016). The flexibility within the peripheral stalk is proposed to smoothen transmission of power between the rotary *c*-ring and the F_1 domain with significant conformational variability of the C-terminal part of subunit *b*, which is in proximity to subunit δ as shown by the atomic resolution structures of the *Geobacillus stearothermophilus* (formerly *Bacillus* PS3) F-ATP synthase (Guo et al., 2018). The genes encoding the *b*-δ subunits of mycobacterial F-ATP synthase are unique, in that the putative *b* subunit (*atpF*) and δ subunit (*atpH*) genes have fused to form a single gene (*atpH*) (Gajadeera and Weber, 2013). In addition, the *atpF* gene of mycobacteria encodes the information for subunit *b'*, which is a shorter *b*-type subunit, without the C-terminus (Fig. 1B).

Additional special features of the mycobacterial F-ATP synthases are the unique 36 amino acid C-terminal extension of the nucleotide-binding subunit α ($Mt\alpha_{514-549}$ according to the *M. tuberculosis* numbering; Fig. 1A) and the novel loop region γ subunit ($Mt\gamma166-179$; Fig. 1A), whose deletions result in significant reduction in ATP synthesis (Hotra et al., 2016; Ragunathan et al., 2017). Also specific for mycobacterial F-ATP synthases are the two shorter α-helices within the C-terminal domain (CTD) of subunit ϵ, which is connected via a linker (amino acids 88–89 according to *M. tuberculosis*) with the N-terminal β-barrel domain (NTD, amino acids 1–87) (Biuković et al., 2013; Joon et al., 2018). Removal of the C-terminal residue D121 of $Mt\epsilon$ (Joon et al., 2018) was found to decrease ATP synthesis.

These unique structural differences of mycobacterial subunits α, γ, and ϵ have also been described to be in part involved in the inability of mycobacterial F-ATP synthases to establish a significant proton gradient during ATP hydrolysis, and/or its low or latent ATPase activity in the fast- or slow-growing form (Haagsma, et al., 2010; Hotra et al., 2016; Kundu et al., 2016; Ragunathan et al., 2017; Joon et al., 2018). Such latency of ATP hydrolysis activity has also been observed for the α-proteobacterium *Paracoccus denitrificans* F-ATP synthase (Perez and Ferguson, 1990; Pacheco-Moisés et al., 2000, 2002; Zharova and Vinogradov, 2003), where the unique ζ-protein is suggested to cause the inhibition (Zarco-Zavala, et al., 2014; García-Trejo, et al., 2016).

So far, the crystallographic structures of the *M. smegmatis* $\alpha_3\beta_3\gamma\epsilon$ complex (Zhang et al., 2019), the *c*-ring of *M. phlei* (Preiss et al., 2015) as well as the solution NMR structure of *M. tuberculosis* subunit ϵ ($Mt\epsilon$) have been determined (Joon et al., 2018) (Fig. 1A). To shed more light into the overall structure of the mycobacterial F-ATP synthase, as well as the structural and mechanistic functions of the unique mycobacterial subunit stretches, a first purification protocol to isolate the entire and enzymatically active *M. smegmatis* F_1F_O ATP synthase is described, providing a platform to determine a low-resolution structure of the enzyme complex by electron microscopy (EM). Genetic engineering enabled the production of a highly pure *M. tuberculosis* *b*-δ fusion subunit (*Mtb*-δ), whose secondary structural content is presented. Given the essential role of the mycobacterial F-ATP synthase for growth, including its unique subunit epitopes, which are potential targets for antitubercular compounds, further structural- and mechanistic features of the mycobacterial peripheral *b*-δ fusion subunit are discussed.

2. Material and Methods

2.1. Biochemicals

Pfu DNA polymerase was purchased from Thermo Scientific (Massachusetts, USA) and Ni^{2+}-NTA chromatography resin was obtained from Qiagen (Hilden, Germany). Enzymatic digestion was performed using restriction enzymes from New England BioLabs. Chemicals from Bio-Rad (California, USA) were used for SDS-PAGE. All other chemicals of analytical grade were obtained from Biomol (Hamburg, Germany), Merck (Darmstadt, Germany), Sigma, or Serva (Heidelberg, Germany), Thermo Fischer (UAS).

2.2. Preparation of the plasma membrane from M. smegmatis mc² 155

In order to purify the plasma membrane (PM) of *M. smegmatis* mc^2 155 for isolation of the F-ATP synthase, cells were cultivated overnight at 37 °C in 7H9 supplemented with 10% ADC, 0.5% glycerol and 0.05% Tween 80 until it reached OD_{600} 0.6–0.7. The culture was expanded in 200 ml supplemented 7H9 and grown in 1-litre shake flasks (100 rpm) until OD_{600} 0.6–0.7. This culture was used to inoculate a 500 ml culture that was grown overnight in 2-litre shake flasks (100 rpm) until an OD_{600} of 0.6–0.7. About 6 g (wet weight) of *M. smegmatis* mc^2 155 were resuspended in 40 ml membrane preparation buffer (50 mM
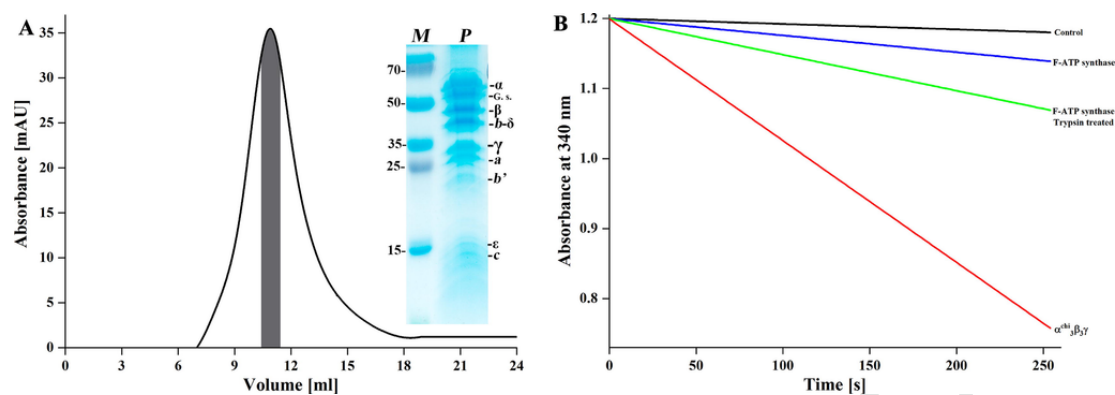
Fig. 2. (*A*) Isolation of the *M. smegamatis* F-ATP synthase using size-exclusion chromatography. The collected fractions at around 10.9 ml are shown in grey. *Inset*, the 17% SDS gel shows the purity and subunit composition of the enzyme (*lane P*). *G.s.*, mycobacterial Glutamine synthetase. (*B*) Continuous ATPase activity of the *M. smegmatis* F-ATP synthase, the *M. smegmatis* F-ATP synthase after treatment with trypsin, and the α^{chi}_3:β_3:γ complex plotted against the time. The graphs are an average of three determinations.
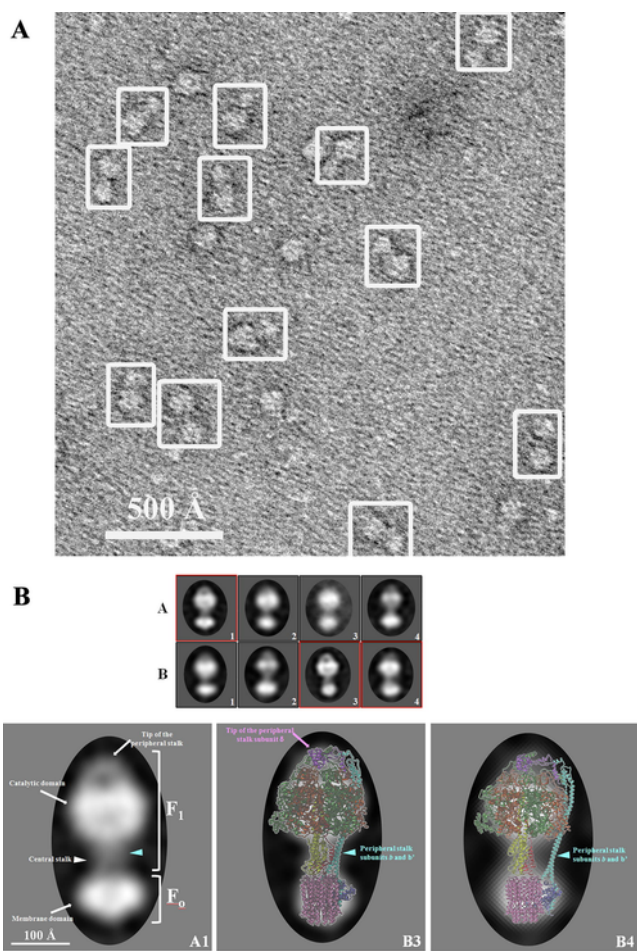

Fig. 3. Negative stained EM of purified *M. smegamatis* F_1F_O ATP synthase. (*A*) Electron micrograph showing the selected particles consisting of two visible domains. (*B*) The gallery shows eight 2D class averages resulting from two rounds of 2D classifications. Classes showing the prominent structural features of the complex are magnified in *A1, B3* and *B4* below. *A1* shows the lateral view of the complex where the F_1 and F_O parts are clearly distinguished. *turkis arrowheads* indicate the mass of the peripheral stalk connecting the F_1 (tip on the top of the F_1 domain) and F_O part. The *white arrowhead* indicates the mass of the asymmetrical central stalk. The *white arrows* indicate the membrane-embedded subunit *a* associated with the *c*-ring and the peripheral stalk. *B3* and *B4* reveal the side-views of the complex with different positions as discerned from the orientation of the mass of the central- and peripheral stalks, reveals the superimposition of the *E. coli* F-ATP synthase (PDB ID: 5T4Q; Sobti et al., 2014) on the projections of the *M. smegmatis* F_1F_O ATP synthase. *light rose arrow* points to the mass of the δ subunit of the *E. coli* F-ATP synthase.

MOPS, 2 mM $MgCl_2$, pH 7.5) containing EDTA-free protease inhibitor cocktail (1 tablet in 20 ml buffer, Roche-USA) and 1.2 mg/ml lysozyme, respectively. The suspension was stirred at room temperature for 45 min and additionally supplemented with 300 μl 1 M $MgCl_2$ and 50 μl DNase I (Thermo Fischer, USA), and continued stirring for another 15 min at room temperature. All subsequent steps were performed on ice. Cells were broken by three passages through ice precooled Model M−110L Microfluidizer processor (M−110L) at 15,000 psi. The suspension containing lysed cells was centrifuged at 15,000 × g at 4 °C for 20 min. The supernatant containing membrane fraction was further subjected to ultracentrifugation at 27,000 × g for 40 min, and 160,000 × g at 4 °C for 1 h with a P50AT2 rotor using the Himac CP90WX ultracentrifuge (HITACHI) to separate the crude mycomembrane-containing cell wall elements from the PM. The supernatant was discarded while the PM fraction was resuspended in the membrane preparation buffer containing 15% glycerol, followed directly with the solubilisation of the F-ATP synthase.

2.3. Purification of the M. Smegamtis mc² 155 F_1F_O ATP synthase

To solubilize the *M. smegamtis* mc² 155 F_1F_O ATP synthase the PMs were dissolved in buffer A (50 mM Tris/HCl, 10 mM $MgCl_2$, 10% [v/v] glycerol, 2 mM $Pefabloc^{SC}$ (4-(2-aminoethyl)benzenesulfonyl fluoride hydrochloride) (BIOMOL), 0.5% [w/v] n–dodecyl–β–maltoside (DDM; Thermo Scientific, UAS), pH 7.5) and incubated for 60 min at 4 °C. Remaining membranes were removed by ultracentrifugation (180,000 × g, 45 min) and the solubilisate was applied to a Ni^{2+}–NTA-chromatography. Ni^{2+}-NTA beads were equilibrated with buffer B (50 mM Tris/HCl, 10 mM $MgCl_2$, 10% [v/v] glycerol, 2 mM $Pefabloc^{SC}$, 0.05% [w/v] DDM, 0.8 mM dithiothreitol (DTT), pH 7.5) prior to incubation with the solubilisate for 1 h at 4 °C by mixing on a sample rotator (Neolab). The material was transferred to a column and the F-ATP synthase was eluted as an unbound fraction, while contaminants binding to the Ni-NTA material were eluted with increasing concentrations of imidazole in buffer B.

Fractions containing the F-ATP ATP synthase were pooled and applied into an ion-exchanger column (Res Q, 6 ml, GE-Healthcare). The F-ATP synthase containing fractions eluted at 250 mM NaCl and were concentrated to a volume of 500 μl (Vivaspin 20 columns, 100 kDa MWCO, Sartorius, Germany), to further purify the sample via an additional size exclusion chromatography (Superdex HR 300 column (GE Healthcare)) at room temperature. The Superdex HR 300 column was equilibrated with buffer B (50 mM Tris/HCl, 10 mM $MgCl_2$, 10% [v/v] glycerol, 0.05% [w/v] DDM, 0.8 mM DTT, pH 7.5). The protein eluted after around 10.9 ml with a flow rate of 0.5 ml/min. Only the major
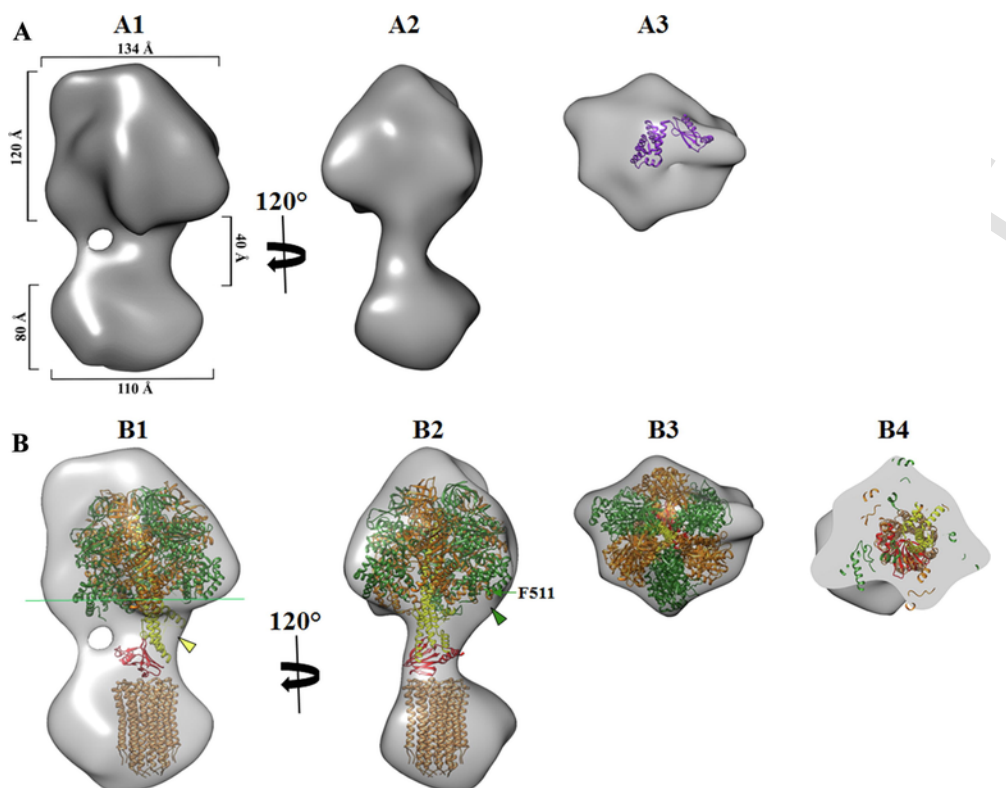
Fig. 4. Surface representation of the 3D reconstruction of the *M. smegmatis* F-ATP synthase refined to about 33.4 Å using *RELION* v*1.4* (Tang et al. 2007) with side views (*A1-A2*) and top view (*A3*). *A3*, reveals subunit δ (*purple*) of the chloroplast F-ATP synthase cryo-EM structure (PDB ID: 6FKF; Hahn et al., 2018) which sits on top of the three α (*green*) subunits (*B3*). *B1-B2* show that the mycobacterial $\alpha_3\beta_3\gamma\varepsilon c$ complex (PDB ID: 6FOC; Zhang et al., 2019; PDB ID: 4V1G; Preiss et al., 2015) fitted into the surface density map obtained from the negative stained EM of the reconstituted *M. smegmatis* F-ATP synthase. The unoccupied volume of the low resolution *M. smegmatis* F-ATP synthase (side-view *B1*) visualizes the volume available for the F_O subunits *a*, the N-terminal and membrane-embedded parts of subunits *b*, *b'*, and the peripheral stalk (*b, b'*), which fuses with the mycobacterial subunit δ at the crown of the F_1 domain. Subunits α, β, γ, ε, and *c* are colored in *green*, *orange*, *yellow*, *red*, and *beige*, respectively. The *yellow arrowhead* in *B1* indicates the missing structural elements in the crystal structure of subunit γ (PDB ID: 6FOC; Zhang et al., 2019). The *green arrow* and *green arrowhead* reveal the last residue F511 of subunit α and the available space for the unresolved residues 512–548 within the subunit α structure of the *M. smegmatis* $\alpha_3\beta_3\gamma\varepsilon$ complex (PDB ID: 6FOC; Zhang et al., 2019), respectively. (*B4*) a cross-section at the distinct C-terminal region of subunit α (*green line* in *B1*) reflects that the additional mass in the 3D reconstruction (*B1-B2*) could be due to the presence of the additional mycobacterial C-terminal stretch residues 512–548. (For interpretation of the references to colour in this figure legend, the reader is referred to the web version of this article.)

fractions from peak 1 were pooled and applied onto a 17% SDS-gel (Laemmli, 1970).

2.4. ATP hydrolysis activity

The ATP hydrolysis activity of *M. smegmatis* mc^2 F-ATP synthase was measured with a continuous assay. In brief, 6 μg of F_1F_O ATP synthase was added at 37 °C to 100 μl of a reaction mix, containing 25 mM Hepes/HCl (pH 7.5), 25 mM KCl, 5 mM MgCl$_2$, 5 mM KCN, 2 mM phosphoenolpyruvate, 2 mM ATP, 0.4 mM NADH, 30 U L-lactic acid dehydrogenase and 30 U pyruvate kinase. The absorbance at 340 nm was observed with a spectrometer for 5 min. The specific activity was determined from the linear slope of the graph.

The effect of trypsin on the ATP hydrolysis of the *M. smegmatis* F-ATP synthase was studied according to the protocol of Zhang et al. (2019). Hereby, purified *M. smegmatis* F-ATP synthase was incubated with bovine trypsin (1 mg/ml) at a trypsin:*M. smegmatis* F-ATP synthase ratio of 1:50 (w/w) for 2 min at 37 °C. Digestion was terminated with a 2-fold molar excess of bovine pancreatic trypsin inhibitor (5 mg/ml).

2.5. Electron microscopy, 2D- and 3D image analysis of M. Smegmatis F-ATP synthase

M. smegmatis mc^2 F-ATP synthase was diluted in buffer B to 80 μg/ml and a volume of 4 μl of protein sample was applied to a glow-dis-

charged carbon coated copper transmission electron microscopy grid and stained with 2% (w/v) uranyl acetate. Electron micrographs were recorded on a Tecnai spirit T12 transmission electron microscope (FEI) equipped with a 4 K CCD camera (FEI) operated at a voltage of 120 kV at a calibrated magnification of 66,350 × under low dose conditions. 80 micrographs were recorded at 0° angle for the enzyme complex. A total of 8400 particles were selected for 2D analysis. The selection criteria were clear visibility of single molecules and separation from neighboring particles. Particles were picked using EMAN2 (Tang et al., 2007) and processed using RELION v1.4. 3D classification and class refinement were performed in *RELION* v1.4 (Scheres, 2012)). A reference density map filtered to 50 Å was generated using the structural coordinates of *E. coli* F-ATP synthase (PDB code 5T4Q; Sobti et al., 2016). Fitting and visualizing of the experimentally acquired surface density map of the *M. smegmatis* F_1F_O ATP synthase complex were all achieved within UCSF Chimera.

2.6. Cloning, production and purification of Mtb-δ

In order to generate the *M. tuberculosis* $b-\delta_{24-446}$ construct ($Mtb-\delta_{24-446}$), which excludes the bases encoding the N-terminal, membrane-embedding amino acids, the respective region of the Open Reading Frame of the *atpH* gene from *M. tuberculosis* HR37v was amplified using primers engineered to contain an *Nde*I restriction site in the forward primer (5'-CGATTTATCCATATGCTCGTAGGGCGTTTG-3') and a *Hind*III restriction site in the reverse primer (5'-CTAG-
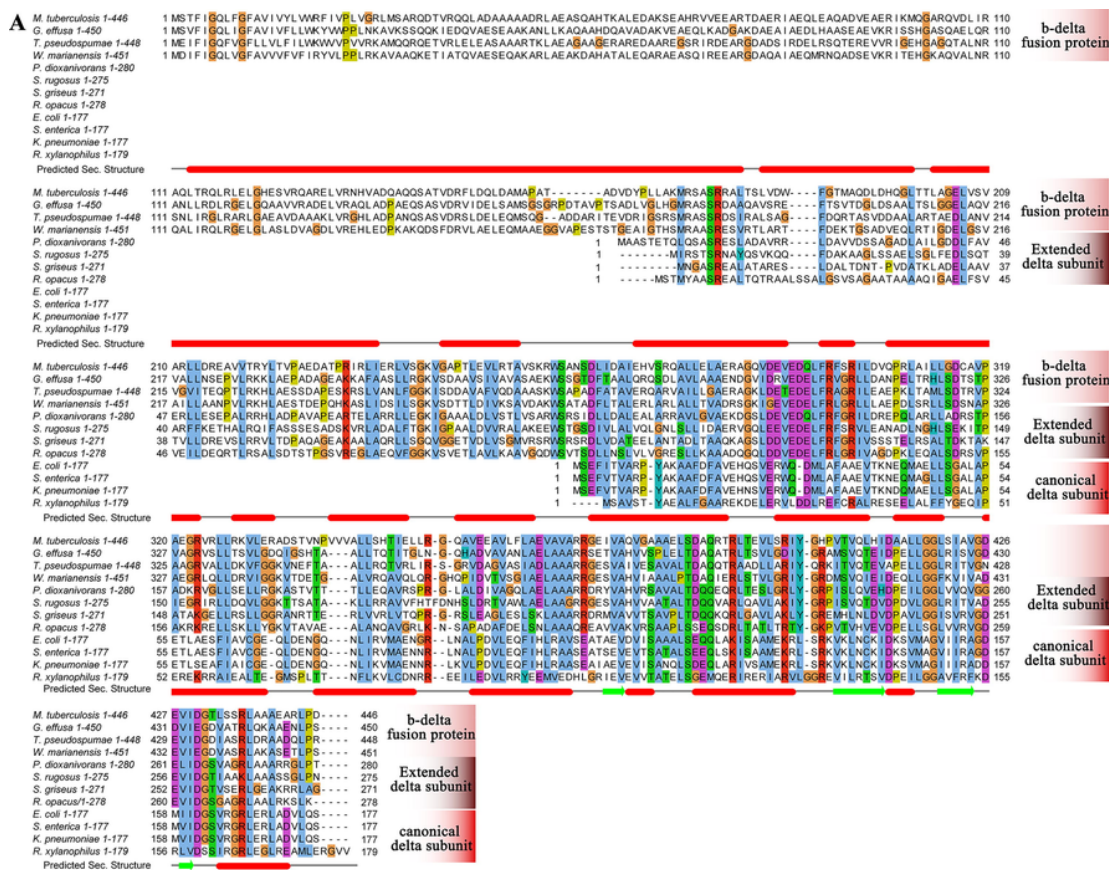
Fig. 5. Amino acids sequence alignments and purification and CD spectroscopy of *Mtb*-δ_{25-446}. (*A*) Multiple sequence alignment of the peripheral subunit *b*-δ, extended δ and the canonical δ from the bacteria domain. The amino acid sequence of the *b*-δ fusion protein of members of the Corynebacteriales suborder (including the genus *Gordonia, Tsukamurella, Williamsia* and *Mycobacterium*) were aligned with the extended δ subunit of the *Actinobacteria phylum* and the canonical δ subunit of other bacteria species. The alignment was performed using Clustal Omega software (Sievers et al., 2011) and visualized using Jalview (Waterhouse et al., 2009). The default Clustal colour scheme was used accordingly to denote conservation and categories of the amino acids. The predicted secondary structure using the *M. tuberculosis* sequence was generated by JnetPred in the Jalview program. The Accession numbers for the selected sequence are as follows; *M. tuberculosis*: WP_031698503.1, *G. effusa*: WP_007316229.1, *T. pseudospumae*: WP_068575214.1, *W. marianensis*: WP_099383244.1, *P. dioxanivorans*: WP_013673849.1, *S. rugosus*: WP_007467277.1, *S. griseus*: WP_030762241.1, *R. opacus*: WP_128641830.1, *E. coli*: WP_097290843.1, *S. enterica*: WP_058106926.1, *K. pneumoniae*: WP_102009146.1, *R. xylanophilus*: WP_011564619.1. (*B*) Elution of the recombinant *Mtb*-δ_{25-446} by a linear gradient of NaCl on anion exchange column (Resource Q 6 ml) with a constant flow rate of 2 ml/min. The fractions of peak 1, indicated by the grey area, where applied onto a 17% SDS-gel (*1*). (*C*) Far UV Circular dichroism spectroscopy of recombinant *Mtb*-δ_{25-446}.

TAAGCTTTCAGTCGGGCAGTCGTGC-3'). The amplified PCR product was then digested with *NdeI/HindIII* restriction enzymes (NEB, MA, USA). It was purified using the gel extraction kit (QIAGEN) as per the manufacturer's protocol and subsequently ligated into the *NdeI* and *HindIII* restriction site of the digested and purified *E. coli*-mycobacterium shuttle vector pYUB1049. The shuttle vector pYUB1049 was kindly provided by Professor Gregory M. Cook (Department of Microbiology, University of Otago, New Zealand). This vector allows the addition of a His-tag and a thrombin cleavage site at the N-terminus. The construct was then transformed into *E. coli* TOP10 cells (Invitrogen, USA) and plated on low salt Luria-Bertani (LB) agar medium

containing 50 µg/ml of hygromycin B. Positive clones were selected and their plasmid prepared using the QIAPrep Spin Miniprep kit (QIAGEN). Plasmids with the desired insets were sent for sequencing to confirm the faithfulness and integrity of the recombination. The respective plasmid was transformed into the *M. smegmatis* mc^2 4517 expression system (Wang et al. 2010).

The expression culture was grown at 37 °C and aliquots of culture were taken at 48 h to check for protein expression. Cells were spun at 7500 × g for 20 min and the cell pellets were resuspended in lysis buffer (50 mM 150 mM NaCl, Tris pH 8.5). The cells were then lysed by sonication on ice 4 × 2 mins using a Misonix Sonicator (U.S.A). The
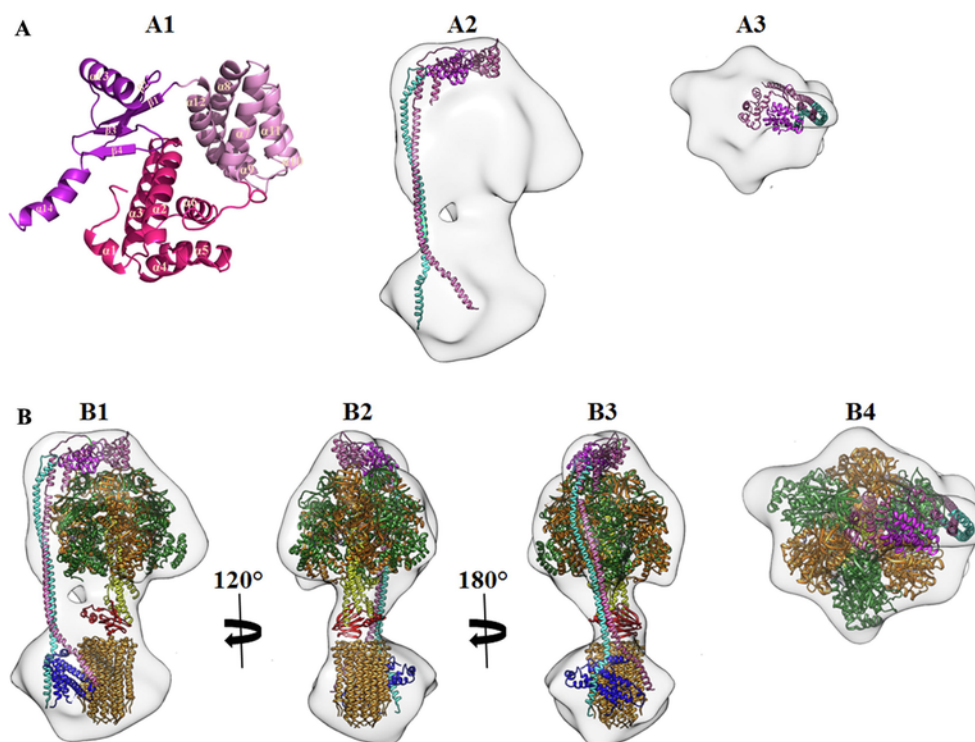
Fig. 6. *Ab-intio* structure of mycobacterial subunit δ and superimposition of the 3D reconstruction of the *M. smegmatis* F-ATP synthase with structural models of its individual subunits. *A1* displays the derived *ab-initio* structure of mycobacterial subunit δ with its N-terminal 111-residues domain (α1-α6) in *hot pink*, the α-helices (α7-α12), which form the N-terminus in canonical δ's in *light pink*, and the C-terminal domain composed of β1-β4 and α13-α14 (*magenta*). *A2* and *A3* show side- and top view with the superimposed *ab-inito* of the fused *b*-d and subunit b' (*turkish blue*), respectively. *B1-B3* show side- and *B4* top views, respectively, that the mycobacterial α$_3$β$_3$γεc complex (PDB ID: 6FOC; Zhang et al., 2019; PDB ID: 4V1G; Preiss et al., 2015) fitted into the surface density map obtained from the negative stained EM of the reconstituted *M. smegmatis* F-ATP synthase. The unoccupied volume of the low resolution *M. smegmatis* F-ATP synthase visualized in Fig. 4 above becomes occupied by the volume of the *ab-initio* structure of mycobacterial subunits *a* (*blue*), the N-terminal and membrane-embedded parts of the mycobacterial subunits *b*, *b'* (in *turkish blue*), and the peripheral stalk (*b*, *b'*), which fuses with the novel mycobacterial subunit δ (*light-* and *hot pink*). The latter occupies well the tip of the F$_1$ domain. The crystallographic structures of subunits α, β, γ, ε, and *c* are colored in *green*, *orange*, *yellow*, *red*, and *beige*, respectively. (For interpretation of the references to colour in this figure legend, the reader is referred to the web version of this article.)

lysate was then spun at 40,000 × *g* to separate soluble and insoluble fractions. The filtered soluble fraction was incubated with Ni^{2+}-NTA agarose beads for 1 h at 4 °C to bind the His$_6$-tagged proteins, which were later eluted with a linear imidazole gradient (0–250 mM) in Buffer A (50 mM Tris/HCl, pH 8.5, 10% glycerol). The eluted fractions were applied on a 17% SDS-PAGE (Laemmli, 1970) to check for the presence of the desired protein. The appropriate fractions were pooled, diluted with Buffer B (50 mM Tris/HCl, pH 8.5 and 10% glycerol) to reduce the salt concentration to 50 mM, and subsequently applied onto an anion-exchange column (Mono Q, 6 ml, GE-Healthcare). The fractions containing recombinant *Mtb*-δ$_{24-446}$ were pooled and concentrated as required using Centricon YM-30 (30 kDa molecular mass cut off) spin concentrators (Millipore).

2.7. Circular dichroism spectroscopy

Steady-state Circular dichroism spectroscopy (CD) spectra were measured in 0.1 mm quartz Hellma cell (60 μl volume) at 18 °C on CHIRASCAN spectropolarimeter (Applied Photophysics) instrument at a step resolution of 1 nm from 180 to 260 nm far UV range, of spectrum under continuous purging of N$_2$ gas. Protein samples were buffer exchanged, reduced or oxidized by appropriate protocols before measurements. The *M. tuberculosis* b-δ$_{25-446}$ fusion protein was measured in triplicates at a concentration of 1.9 mg/ml, with the buffer reading taken before and after protein sample. Averaged buffer base line was subtracted from average protein values using in built Chirascan software. Initial degree cm^2·dmol^{-1} units were converted into mean molar residue ellipticity (Θ) with the help of Chirascan software by giving appropriate cell path length, molecular weight, number of amino acid

residues and protein concentration values. In order to analyze the CD spectrum, the programs Dicroprot (Deléage et al., 1993) and Neural Net (Böhm et al., 1992) were used.

2.8. Computational details

The sequence of the *b'* and fused *b*-δ subunits of *M. smegmatis* were retrieved from UniProt (A0R200 and A0R203 respectively) and aligned against the sequence of *E. coli* b and δ subunits derived from the PDB template 5T4Q (Sobti et al., 2016) using *mafft* (Katoh and Standley, 2013) with the L-ins-I alignment strategy. Alignment resulted in a good overlap of fused *M. smegmatis* b-δ with both F$_O$-b and F$_1$-δ in the N-terminal and C-terminal regions, respectively. The alignment is provided as a Supplementary file (Supplementary Fig. 1). A region of 111 additional residues is present in fused b-δ for which a BLAST search was performed, but no structural templates could be identified. Hence, we proceeded to use the Robetta *ab-initio* structure prediction server, based on the *Rosetta* (Das & Baker, 2008) suite of modeling tools, to predict the structure of this region. The resulting structures consistently show a fold containing five α helices. Five structure models were obtained and attempted to fit with the geometry of F$_O$-b and F$_1$-δ of *E. coli* structure 5T4Q (Sobti et al., 2016). The predicted fold fits well with a lightly structured region at the C-terminus of F$_1$-δ. The model whose termini best aligned with the existing template was chosen and positioned to connect with F$_O$-b and F$_1$-δ to create a full structural template for the fused b-δ model. Subsequently, we used the alignment obtained previously in conjunction with this structure as an input for homology modeling. Modeler 9.19 (Eswar et al., 2006) was used with default settings of the *automodeller* plugin and 100 structures were generated, out
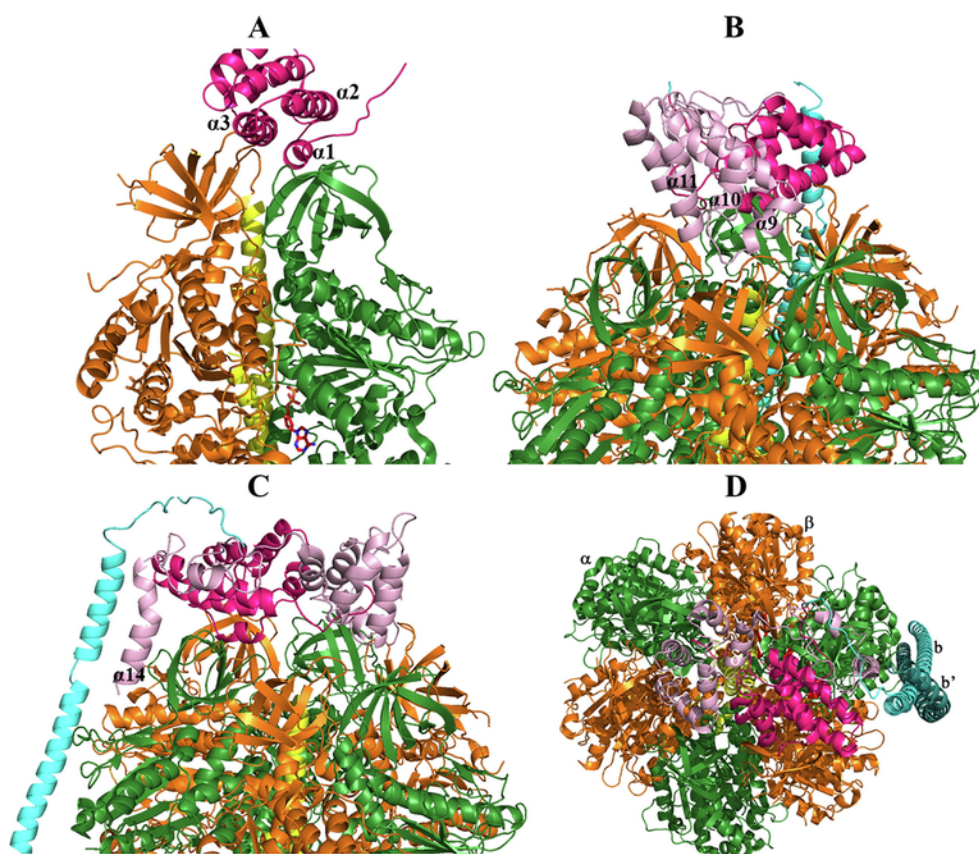
Fig. 7. The relative arrangement of mycobacterial subunit δ to the $\alpha_3\beta_3$ head. (*A*) The helices α1 and α3 of the 111-residues extension of the *ab-initio* determined mycobacterial δ are predicted to be in proximity to the interface of the N-termini of one α-β pair within the crystallographic structure of the *M. smegmatis* F_1-ATPase (Zhang et al., 2019). (*B*) Helix α9 and α11 are proposed to be in the neighborhood to the N-termini of subunit β (β3) and α (α3), respectively, (*C*) while α-helix 14 is in proximity to subunit α (α1). The crystallographic structures of subunits α and β are colored in *green* and *orange*, respectively, while the *ab-initio* determined mycobacterial subunit *b* is displayed in *turkish blue*. (*D*) The top view shows the fused *b*-δ sitting on top of α_3:β_3 crown of the *M. smegmatis* F-ATP synthase. (For interpretation of the references to colour in this figure legend, the reader is referred to the web version of this article.)

of which the model with the lowest RMSD to the template was chosen. We then replaced the F_O-*b* and F_1-δ segments of 5T4Q (Sobti et al., 2016) with the newly modeled structure and proceeded to fit it with the electron density map described in this study. The fused *b*-δ segment including the *ab initio* modeled extended *b* fit well with observed density, as shown in Fig. 6.

3. Results and discussion

3.1. Isolation of a complete M. Smegmatis F_1F_O ATP synthase

Since disruption of the mycobacterial cells with high fluid pressure remains the best lysis method for obtaining significant amounts of PM fractions from these bacteria (Rezwan et al., 2007), 6 g of *M. smegmatis* mc^2 155 were resuspended in buffer (50 mM MOPS, 2 mM MgCl$_2$, pH 7.5, EDTA-free protease inhibitor and 1.2 mg/ml lysozyme) and broken by three passages through a Microfluidizer (see details in Material and Methods). The suspension containing lysed cells was centrifuged at $15,000 \times g$ as described recently (Ragunathan et al., 2017), followed by subsequent ultracentrifugation steps at $27,000 \times g$ and $160,000 \times g$ to separate the crude mycomembrane-containing cell wall elements from the PM. To solubilize the mycobacterial F-ATP synthase the PM pellet was dissolved in buffer containing 0.5% [w/v] n–dodecyl–β–maltoside (DDM), incubated for 1 h, and remaining membranes were removed by ultracentrifugation ($180,000 \times g$) and the solubilisate was applied to a Ni^{2+}-NTA-chromatography, to separate contaminants binding to the affinity column. To further remove impurities, we introduced an ion–exchange column (Resource^{TM} Q column) and a size exclusion chromatography step (Superdex 300 column). The elution profile showed one major peak (Fig. 2A). Fractions from this peak contained *M. smegmatis* F-ATP synthase with all subunits (Fig. 2A). The identity of major subunit α, β, γ and the mycobacterial specific fused *b*-δ was established using MALDI mass spectrometry (Supplementary Tables S1A–D). These studies revealed that the 59 kDa, 52 kDa, 48 kDa, and 34 kDa band corresponds to subunit α, β, *b*-δ, and the rotary subunit γ (Fig. 2B; Supplementary Tables S1A–D). The band at 54 kDa was identified to contain the mycobacterial Glutamine synthetase (Supplementary Table S1E).

3.2. ATP hydrolysis traits of the M. smegmatis F_1F_O ATP synthase

The isolated *M. smegmatis* F-ATP synthase was used for electron microscopy imaging (see below) and enzymatic assays (Fig. 2B). The ATP hydrolysis activity of this complex was $0.4 \pm 0.1 \, \mu\text{mol min}^{-1}$ (mg protein)$^{-1}$, slightly higher compared to the ATPase activity of about $0.04 \pm 0.01 \, \mu\text{mol min}^{-1}$ (mg total protein)$^{-1}$ of the *M. smegmatis* F-ATP synthase within inverted membrane vesicles (IMVs) determined recently (Ragunathan et al., 2017), and to the activity of the recombinant *M. smegmatis* F_1 ATPase (α_3:β_3:γ:ε) of about $0.07 \, \mu\text{mol min}^{-1}$ (mg protein)$^{-1}$ (Zhang et al., 2019). In comparison, the ATP hydrolysis activity of the α^{chi}_3:β_3:γ complex was determined to be $3.4 \pm 0.07 \, \mu\text{mol/min/mg}$ protein (Fig. 2B), which is comparable to that determined in previous studies (Ragunathan et al., 2017; Bogdanović et al., 2019), and reflects the low ATP hydrolysis activity of the mycobacterial F-ATP synthase described previously (Haagsma et al., 2010; Hotra et al.,
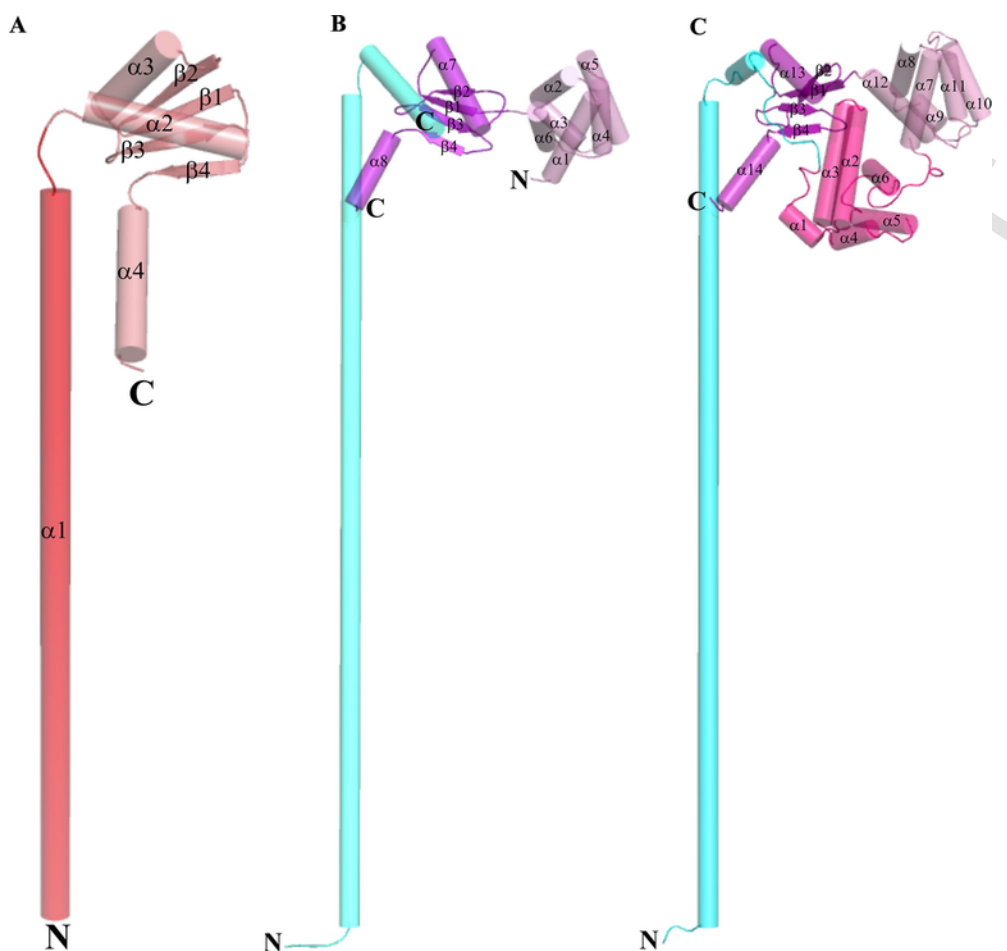
Fig. 8. Similarities and diversities of structural features within the evolutionary related A-ATP synthase peripheral stalk subunit E, the canonical- and mycobacterial subunit δ of F-ATP synthases. (*A*) The topological arrangement of the peripheral subunits E of the *Pyrococcus horikoshii* OT3 A-ATP synthase reveals its N-terminal helix α1 which continues into the globular domain (Balkrishna et al., 2012). The latter is composed of α2-α3, the β1-β4 stretch, followed by the C-terminal helix α4. (*B*) Subunit *b* of the chloroplast F-ATP synthase (Hahn et al., 2018) is equivalent to the N-terminal stator element α1 of subunit E of A-ATP synthases. In comparison, this canonical δ subunit consists of a similar C-terminal domain with a β1-β4 and very C-terminal α helix arrangement as observed for the archaeal subunit E, while its N-terminus contains a bundle of α-helices. (*C*) The topological arrangement represented by the *ab-initio* structure of the mycobacterial subunit δ highlights the novel N-terminal 111-residues extension, providing additional contacts to the α3β3 headpiece essential for stability for the two rotary elements within the engine and may in part contribute to an efficient transfer of elastic energy.

2016). Considering the aspects of protein concentration determination of soluble, detergent-solubilized and membrane-embedded complexes, the data also indicate that no drastic difference can be observed between the ATP hydrolysis activity of the membrane-embedded, DDM-solubilized F-ATP synthase as well as the F₁-ATPase.

Because of the presented low ATP hydrolase activity of the isolated *M. smegmatis* F₁F₀ ATP synthase as well as the described recombinant *M. smegmatis* F₁-ATPase (Zhang et al., 2019), which can not be stimulated by lauryldimethylamine oxide (LDAO), but by trypsin cleavage (Zhang et al., 2019), the *M. smegmatis* F₁F₀ ATP synthase was pretreated with trypsin according to Zhang et al., (2019) and an ATP hydrolysis activity of $0.8 \pm 0.1\,\mu\mathrm{mol\,min}^{-1}$ (mg protein)$^{-1}$ was determined (Fig. 2B). Taken together, the data reflect that an enzymatically active and entire *M. smegmatis* F₁F₀ ATP synthase was isolated.

3.3. Electron microscopy and three-dimensional reconstruction

The negatively-stained enzyme, prepared for electron microscopy, yielded dispersed single particles (Fig. 3A). The negatively stained *M. smegmatis* F-ATP synthase shows a preferred orientation on the electron microscope grids with its long axis lying in the plane of the carbon support film (Fig. 3A). A total of 8400 particles were subjected to image processing. After two rounds of particle elimination and classification, 3335 particles were used for 2D class averaging to generate the *M. smegmatis* F-ATP synthase projections. All of the resulting projections revealed a tripartite structure consisting of the F₁ headpiece, a membrane-embedded domain, F₀, and the connecting central- and peripheral stalks, including the tip on the top of the F₁-domain formed by the fused *b*-δ (Fig. 3B). The averaged classes were separated based on the orientation of the asymmetrical central stalk, the asymmetrical F₀ domain (subunit *a* and the *c*-ring) and/or the visibility of the peripheral stalk connecting the F₁ and the F₀ domains. The entire *M. smegmatis* F-ATP synthase extends to a length of around 240 Å. In the second class (Fig. 3B-A1), the peripheral stalk is shown to extend upward and downward to contact subunit δ of F₁ and subunit *a* of F₀, respectively, whose densities are indicated with the arrows (Fig. 3B-A1, 3B-B3, and 3B-B4). Besides the peripheral stalk, mass contributing to the central stalk is visible as well. The data presented confirm that a stable and well assembled *M. smegmatis* F-ATP synthase was isolated.

The final three-dimensional reconstruction (Fig. 4) was calculated from the two-dimensional class averages (Fig. 3B). The resolution was determined to be 33.4 Å by the Fourier shell correlation criterion with a threshold of 0.143 times the noise correlation value (Supplementary Fig. 2). The dimensions of the F₁ headpiece, the central stalk domain, and the membrane part, F₀, are approximately 120×134, 40×70,

and 80×110 Å, respectively (Fig. 4A1-2). The final reconstruction visualized the peripheral stalk connecting the membrane-embedded F_O domain (Fig. 4A1, B1-2) and moving up on top of the $\alpha_3\beta_3$ crown forming the "tip-volume" (Fig. 4B1-3). Superimposition of subunit δ of the chloroplast F-ATP synthase cryo-EM structure (PDB ID: 6FKF; Hahn et al., 2018) fills a part of this volume and brings this subunit in the vicinity to the N-terminal crown of the three nucleotide-binding subunit α (Fig. 4A3).

The final *M. smegmatis* F-ATP synthase reconstruction accommodates the *M. smegmatis* $\alpha_3\beta_3\gamma\epsilon$ complex- (PDB ID: 6FOC; Zhang et al., 2019) and *c*-ring structure of *M. phlei* (PDB ID: 4V1G; Preiss et al., 2015) (Fig. 4B1-3). The comparison highlights the space lacking at the bottom of subunit α inside the 3D reconstruction of the entire F-ATP synthase (Fig. 4B2), which may be due to the unresolved C-terminal stretch of 37 residues in subunit α of the *M. smegmatis* $\alpha_3\beta_3\gamma\epsilon$ structure (Zhang et al., 2019). In *M. smegmatis*, *M. phlei* and *M. ulcerans* this C-terminal region of amino acids 512–548 is predicted to be disordered, while in *M. bovis* or *M. tuberculosis* it is proposed to include an α-helix (Zhang et al., 2019), as shown for the NMR structure of the α-helical residue 526–539 within the C-terminal peptide $\alpha_{521-540}$ from *M. tuberculosis* ($Mt\alpha_{520-540}$) (Ragunathan et al., 2017). A cross-section at the distinct C-terminal region of subunit α reflects that the additional mass in the 3D reconstruction could be due to the presence of the additional mycobacterial C-terminal stretch (Fig. 4B3). Similarly, a comparison of the top of the *M. smegmatis* $\alpha_3\beta_3\gamma\epsilon$ structure and the 3D reconstruction of the *M. smegmatis* F-ATP synthase highlights the space available to anchor the mycobacterial *b*-δ subunit (Fig. 4B3).

3.4. Production, purification and characterization of the fused b-δ subunit

Our sequence analysis of the *Actinobacteria* phylum, to which *Mycobacteria* belong, highlights variations in the δ subunit (Fig. 5A). Whereas, some early branching *Actinobacteria* such as the *Rubrobacter xylanophilus* (Gao and Gupta, 2012) present a canonical δ subunit consisting of 179 amino acids, which is similar in length to the *E. coli* δ subunit, the *Streptomyces* and *Mycobacteria* species possess a more elongated δ subunit, due to an N-terminal 111 amino acid extension as in the case of *M. smegmatis*, resulting in a 272 amino acids protein. Furthermore, in the case of mycobacteria, there is a fusion between the extended δ and the *b* subunit leading to the *b*-δ fusion protein (446 residues according to *M. tuberculosis*).

To demonstrate that a fused *b*-δ protein is encoded by the *atpH* gene and to characterize its secondary structural content in solution, the *M. tuberculosis* *b*-δ_{25-446} fusion protein was generated, excluding the predicted 24 amino acids of the hydrophobic transmembrane domain of *b*-δ. Mtb-δ_{25-446} was produced in the *M. smegmatis* mc²4517 strain and isolated to high quality and quantity using Ni-NTA-affinity- and ion-exchange chromatography (Fig. 5B). The proper secondary folding of the recombinant Mtb-δ_{25-446} was studied by circular dichroism spectroscopy, measured between 189 and 260 nm (Fig. 5C). The concentration of the purified recombinant protein δ was 1.9 mg/ml in buffer 50 mM Tris/HCl (pH 8.5) and 150 mM NaCl. The maximum at 192 nm and the minima at 210 and 222 nm indicate the presence of mainly α-helical structures in the protein. The average secondary structure content was 69.2% α-helix, 6.6% β-sheet, and 24.2% random coil. These results are consistent with secondary structure predictions based on the subunit Mtb-δ_{25-446} amino-acid sequence, and the β-sheet content is reflective of the amount observed in the four-stranded β-sheets of the CTD of the chloroplast δ subunit (Hahn et al., 2018). The molar ellipticity values at 208 nm and at 222 nm are in a ratio of 0.93.

3.5. The peripheral stalk within the mycobacterial F-ATP synthase

With the input of the secondary structural information of the mycobacterial δ_{25-446} described above and the structural models of the *E. coli* (Sobti et al., 2016) and chloroplast δ (Hahn et al., 2018) an *ab-initio* structural model of the mycobacterial δ subunit with its extended N-terminal 111 amino acids region as well as the subunits *b* and *b'* (Fig. 6A-C) was generated (see Material and Methods). Like the *E. coli*- and chloroplast subunit δ, the mycobacterial counterpart displayed a similar bundle of six short α-helices (α7-α12), followed by the four-stranded mixed β-sheet (β1-β4) and two α helices (α13-α14) at the C-terminal domain (Fig. 6A, -7). Interestingly, the N-terminal 111-residues extension consists of six α-helices (α1-α6). The *ab-initio* model of the subunit δ extension resulted in a configuration that readily accommodates connectivity to the distinct *b* and δ subunits, which is consistent with the density observed in the 3D EM structure of the *M. smegmatis* F-ATP synthase, by filling the tip volume of the $\alpha_3\beta_3$ crown (the correlation coefficient being 0.918 as calculated using Chimera program; (Fig. 6A2-A3, 6B1-B4)), which was only partially occupied by the canonical chloroplast δ (Fig. 4A3). In this configuration, the helices α1 and α3 of the 111-residues extension would come in proximity to the interface of the N-termini of one α-β pair (α1β1), forming the catalytic interface within the crystallographic structure of the *M. smegmatis* F_1-ATPase (Zhang et al., 2019; Fig. 7A). In addition, helix α9 and α11 are in the neighborhood to the N-termini of subunit β (β3) and α (α3) (Fig. 7B), respectively, while the α-helix 14 is in proximity to subunit α (α1) (Fig. 7C-D). In comparison, the canonical subunit δ within the *E. coli*- (Sobti et al., 2016) and chloroplast F-ATP synthase (Hahn et al., 2018) or its mitochondrial equivalent OSCP of the yeast *Yarrowia lipolytica* (Hahn et al., 2016) or *Saccharomyces cerevisiae* (Srivastava et al., 2018) interact only with the α subunits via helices corresponding to the mycobacterial helix bundle (α7-α12; Hahn et al., 2016, 2018).

Finally, the *ab initio* model of the peripheral stalk displayed subunit *b* and *b'* to form a right-handed coiled coil, whose N-termini contribute to the membrane-embedded F_O-domain (Fig. 6A2, B1). Together with the subunit *a*, they fill the remaining volume within the mycobacterial F-ATP synthase EM map (Fig. 6B1-B3).

3.6. An evolutionary view to the topological variations of the peripheral stalk

The canonical δ, as well as OSCP, are described to be essential for the assembly of the *b*-dimer with the rest of the entire engine and therefore to connect the F_1- with the F_O-rotor elements (reviewed in Colina-Tenorio et al, 2018). This enables the peripheral stalk subunits δ and *b* to provide transient elastic energy during the rotary catalytic cycle. This assumption has been made based on the determined heterodimeric right-handed coiled-coil structure of the peripheral stalk subunits E–H of the archaea-type ATP synthases (Lee, et al. 2010; Balakrishna et al. 2012), which consists of the two peripheral stalk subunits E and G. The structure of subunit E (equivalent to subunit *b* in F-ATP synthases) reveals an extended S-shaped N-terminal α-helix, followed by a globular head group (Fig. 8A). The latter is made up of four-stranded β-sheets and two α-helices, followed by a C-terminal α-helical tail (Lee, et al. 2010; Balakrishna et al. 2012), a structural content similar to the C-terminal domain of the canonical subunit δ (Hahn et al., 2018; Guo et al., 2018; Fig. 8B). Because of the essential functions of δ as an anchor of the peripheral stalk at the top of F_1 and its partial contribution to the transient elastic energy during rotation, evolution may have extended the mycobacterial δ to adapt to specific mechanistic and/or regulatory needs (Fig. 8C). As reflected by the peripheral stalk subunit of the related V_1V_O-ATPase, disruption of the

α-helical subunit G (equivalent to subunit *b*) provides the stalk some degree of movement to the complex, and enables the enzyme to dis- or reassemble the V_1- and V_O sector (Oot et al., 2017). The mechanistic importance of the peripheral stalk and in particular the subunit δ homologue, OSCP in mitochondria is revealed to be a target of the insecticide dichlorodiphenyltrichloroethane (DDT) (Younis et al., 2011), the compound Bz-423, which induces apoptosis (Stelzer et al., 2009), as well as the estrogen 17β-estradiol (Zheng et al., 1999). In this context, the mycobacterial δ subunit with its unique N-terminal extension and arrangement within the F-ATP synthase, promises to be an interesting drug target.

4. Conclusion

The purification protocol developed here enabled the enzymatic characterization and visualization of the entire *M. smegmatis* F-ATP synthase with its characteristic $\alpha_3\beta_3$-headpiece, a central and peripheral stalk both connecting the catalytic $\alpha_3\beta_3$ with the membrane-embedded F_O domain. The overexpressed peripheral stalk subunit *Mtb*-$\delta_{25\text{-}446}$ demonstrated that the peripheral stalk subunit *b* and δ are fused via a 111-residues linker region, forming a mainly α-helical protein (69.2% α-helix). Combining these structural insights with the existing structures of the mycobacterial F-ATP synthase ($\alpha_3\beta_3\gamma\varepsilon$ (Zhang et al., 2018), *c*-ring (Preiss et al., 2015), and *Mt*ε (Joon et al. (2018), a structural model of the $\alpha_3\beta_3\gamma\varepsilon ab$-$\delta b'c_9$ ensemble was computed, providing a comprehensive insight into the arrangement of the subunit ensemble and in particular the N-terminal 111-residues stretch at the tip of the catalytic $\alpha_3\beta_3$ headpiece, predicted to be an additional epitope to probe as attractive drug target for TB.

Uncited references

Delaglio et al. (1995), DeLano (2000), Deléage and Geourjon (1993), Pettersen et al. (2004), Ragunathan et al. (2016), Schneider et al. (2012), Shirakihara et al. (2015), Tsumuraya et al. (2009), Uhlin et al. (1997).

CRediT authorship contribution statement

Neelagandan Kamariah: Writing - original draft, Writing - review & editing. **Roland G. Huber:** Writing - original draft, Writing - review & editing. **Wilson Nartey:** Writing - original draft, Writing - review & editing. **Shashi Bhushan:** Writing - review & editing. **Peter J. Bond:** Writing - review & editing. **Gerhard Grüber:** Writing - original draft, Writing - review & editing.

Declaration of Competing Interest

None.

Appendix A. Supplementary data

Supplementary data to this article can be found online at https://doi.org/10.1016/j.jsb.2019.05.008.

References

Balakrishna, A.M., Hunke, C., Grüber, G., 2012. The structure of subunit E of the Pyrococcus horikoshii OT3 A-ATP synthase gives insight into the elasticity of the peripheral stalk. J. Mol. Biol. 420, 155–163.

Biuković, G., Basak, S., Manimekalai, M.S.S., Rishikesan, S., Roessle, M., Dick, T., Rao, S., Hunke, C., Grüber, G., 2013. Variations of Subunit epsilon of the Mycobacterium tuberculosis $_F1_F$O ATP Synthase and a Novel Model for Mechanism of Action of the Tuberculosis Drug TMC207. Antimicrob. Agents Chemother. 57, 168–176.

Böhm, G., Muhr, R., Jaenicke, R., 1992. Quantitative analysis of protein far UV circular dichroism spectra by neural networks. Protein Eng. 5, 191–195.

Capaldi, R.A., Aggeler, R., Wilkens, S., Grüber, G., 1996. Structural changes in the gamma and epsilon subunits of the Escherichia coli $_F1_F$O-type ATPase during energy coupling. J. Bioenerg. Biomembr. 28, 397–401.

Colina-Tenorio, L., Dautant, A., Miranda-Astudillo, H., Giraud, M.-F., González-Halphen, D., 2018. The peripheral stalk of rotary ATPase. Front. Physiol. 9, 1243. https://doi.org/10.3389/fphys.2018.01243.

Cook, G.M., Hards, K., Vilcheze, C., Hartman, T., Berney, M., 2014. Energetics of respiration and oxidative phosphorylation in mycobacteria. Microbiol. Spectr. 2, https://doi.org/10.1128/microbiolspec.MGM2-0015-2013, Epub 2014/10/28.

Das, R., Baker, D., 2008. Macromolecular modeling with rosetta. Annu. Rev. Biochem. 77, 363–382.

Delaglio, F., Grzesiek, S., Vuister, G.W., Zhu, G., Pfeifer, J., Bax, A., 1995. NMRPipe: a multidimensional spectral processing system based on the UNIX pipes. J. Biomol. NMR 6, 277–293.

DeLano, W., 2000. The PyMOL Molecular Graphics System. DeLano Scientific.

Deléage, G., Geourjon, C., 1993. An Interactive Graphic Program for Calculating the Secondary Structure Content of Proteins from Circular Dichroism Spectrum. Oxford University Press.

Diez, M., Zimmermann, B., Börsch, M., Konig, M., Schweinberger, E., Steigmiller, S., Reuter, R., Felekyan, S., Kudryavtsev, V., Seidel, C.A., Gräber, P., 2004. Proton-powered subunit rotation in single membrane-bound F_0F_1-ATP synthase. Nat. Struct. Mol. Biol. 11, 135–141.

Eswar, N., Webb, B., Marti-Renom, M.A., Madhusudhan, M.S., Eramian, D., Shen, M.S., Pieper, U., Sali, A., 2006. Comparative Protein Structure Modeling Using Modeller. Curr. Protoc. Bioinformatics 15, 5–6.

Gajadeera, C.S., Weber, J., 2013. Escherichia coli F_1F_0-ATP synthase with a b/δ fusion protein allows analysis of the function of the individual b subunits. J. Biol. Chem. 288, 26441–26447.

Gao, B., Gupta, R.S., 2012. Phylogenetic framework and molecular signatures for the main clades of the phylum Actinobacteria. Microbiol. Mol. Biol. Rev. 76, 66–112.

García-Trejo, J.J., Zarco-Zavala, M., Mendoza-Hoffmann, F., Hernández-Luna, E., Ortega, R., Mendoza-Hernández, G., 2016. The inhibitory mechanism of the ζ subunit of the F_1F_0-ATPase nanomotor of Paracoccus denitrificans and related α-proteobacteria. J. Biol. Chem. 291, 538–546.

Guo, H., Rubinstein, J.L., 2018. Cryo-EM of ATP synthases. Curr. Opi. Struct. Biol. 52, 71–79.

Haagsma, A.C., Driessen, N.N., Hahn, M.M., Lill, H., Bald, D., 2010. ATP synthase in slow- and fast-growing mycobacteria is active in ATP synthesis and blocked in ATP hydrolysis direction. FEMS Microbiol. Lett. 313, 68–74.

Hahn, A., Parey, K., Bublitz, M., Mills, D.J., Zickermann, V., Vonck, J., Kühlbrandt, W., Meier, T., 2016. Structure of a complete ATP synthase dimer reveals the molecular basis of inner mitochondrial membrane morphology. Mol. Cell 63, 445–456.

Hahn, A., Vonck, J., Mills, D.J., Meier, T., Kühlbrandt, W., 2018. Structure, mechanism, and regulation of the chloroplast ATP synthase. Science 360, 620.

Hotra, A., Suter, M., Biuković, G., Ragunathan, P., Kundu, S., Dick, T., Grüber, G., 2016. Deletion of a unique loop in the mycobacterial F-ATP synthase gamma subunit sheds light on its inhibitory role in ATP hydrolysis-driven H(+) pumping. FEBS J. 283, 1947–1961.

Joon, S., Ragunathan, P., Sundararaman, L., Nartey, W., Kundu, S., Manimekalai, M.S.S., Bogdanović, N., Dick, T., Grüber, G., 2018. The NMR solution structure of Mycobacterium tuberculosis F-ATP synthase subunit ε provides new insight into energy coupling inside the rotary engine. FEBS J. 285, 1111–1128.

Katoh, K., Standley, D.M., 2013. MAFFT multiple sequence alignment software version 7: improvements in performance and usability. Mol. Biol. Evol. 30, 772–780.

Kundu, S., Biuković, G., Grüber, G., Dick, T., 2016. Bedaquiline targets the ε subunit of mycobacterial F-ATP synthase. Antimicrob. Agents Chemother. 60, 6977–6979.

Laemmli, U.K., 1970. Cleavage of structural proteins during the assembly of the head of bacteriophage T4. Nature 227, 680–685.

Lee, L.K., Stewart, A.G., Donohoe, Bernal, R.A., Stock, D., 2010. The structure of the peripheral stalk of Thermus thermophilus ^{H}+-ATPase/synthase. Nat. Struct. Mol. Biol. 17, 373–378.

Lu, P., Lill, H., Bald, D., 2014. ATP synthase in mycobacteria: special features and implications for a function as drug target. BBA 1837, 1208–1218.

Noji, H., Yasuda, R., Yoshida, M., Kinosita Jr., K., 1997. Direct observation of the rotation of F_1-ATPase. Nature 386, 299–302.

Oot, R.A., Couoh-Cardel, S., Sharma, S., Wilkens, S., 2017. Breaking up and making up: the secret life of the vacuolar H+-ATPase. Protein Sci. 26, 896–909.

Pacheco-Moisés, F., García, J.J., Rodríguez-Zavala, J.S., Moreno-Sánchez, R., 2000. Sulfite and membrane energization induce two different active states of the Paracoccus denitrificans F_0F_1-ATPase. Eur. J. Biochem. 267, 993–1000.

Pacheco-Moisés, F., Minauro-Sanmiguel, F., Bravo, C., García, J.J., 2002. Sulfite inhibits the F_1F_0-ATP synthase and the F_1F_0-ATPase of Paracoccus denitrificans. J. Bioenerg. Biomembr. 34, 269–278.

Perez, J.A., Ferguson, S.J., 1990. Kinetics of oxidative phosphorylation in Paracoccus denitrificans. 1. Mechanism of ATP synthesis at the active site(s) of F_0F_1-ATPase. Biochemistry 29, 10503–10518.

Pettersen, E.F., Goddard, T.D., Huang, C.C., Couch, G.S., Greenblatt, D.M., Meng, E.C., Ferrin, T.E., 2004. UCSF Chimera–a visualization system for exploratory research and analysis. J. Comput. Chem. 25, 1605–1612.

Preiss, L., Langer, J.D., Yildiz, , Eckhardt-Strelau, L., Guillemont, J.E., Koul, A., Meier, T., 2015. Structure of the mycobacterial ATP synthase Fo rotor ring in complex with the anti-TB drug bedaquiline. Sci. Adv. 1, e1500106.

Ragunathan, P., Sielaff, H., Sundararaman, L., Biuković, G., Manimekalai, M.S.S., Singh, D., Kundu, S., Wohland, T., Frasch, W., Dick, T., Grüber, G., 2016. The uniqueness of subunit α of mycobacterial F-ATP synthases: an evolutionary variant for niche adaptation. J. Biol. Chem. 292, 11262–11279.

Sassetti, C.M., Boyd, D.H., Rubin, E.J., 2003. Genes required for mycobacterial growth defined by high density mutagenesis. Mol. Microbiol. 48, 77–84.

Scheres, S.H., 2012. RELION: implementation of a Bayesian approach to cryo-EM structure determination. J. Struct. Biol. 180, 519–530.

Schneider, C.A., Rasband, W.S., Eliceiri, K.W., 2012. NIH Image to ImageJ: 25 years of image analysis. Nat. Meth. 9, 671–675.

Shirakihara, Y., Shiratori, A., Tanikawa, H., Nakasako, M., Yoshida, M., Suzuki, T., 2015. Structure of a thermophilic F1-ATPase inhibited by an epsilon-subunit: deeper insight into the epsilon-inhibition mechanism. FEBS J. 282, 2895–2913.

Sievers, F., Wilm, A., Dineen, D.G., Gibson, T.J., Karplus, K., Li, W., Lopez, R., McWilliam, H., Remmert, M., Söding, J., Thompson, J.D., Higgins, D.G., 2011. Fast, scalable generation of high-quality protein multiple sequence alignments using Clustal Omega. Mol. Syst. Biol. 7, 539. https://doi.org/10.1038/msb.2011.75.

Sobti, M., Smits, C., Wong, A.S.W., Ishmukhametov, R., Stock, D., Sandin, S., Stewart, A.G., 2016. Cryo-EM structures of the autoinhibited E. coli ATP synthase in three rotational states. eLife 5, e21598.

Srivastava, A.P., Luo, M., Zhou, W., Symersky, J., Bai, D., Chambers, M.G., Faraldo-Gómez, José D., Liao, L., Mueller, D.M., 2018. High-resolution cryo-EM analysis of the yeast ATP synthase in a lipid membrane. Science 360, eaas9699.

Tang, G., Peng, L., Baldwin, P.R., Mann, D.S., Jiang, W., Rees, I., Ludtke, S.J., 2007. EMAN2: an extensible image processing suite for electron microscopy. J. Struct. Biol. 157, 38–46.

Tsumuraya, M., Furuike, S., Adachi, K., Kinosita Jr., K., Yoshida, M., 2009. Effect of epsilon subunit on the rotation of thermophilic Bacillus F1-ATPase. FEBS Lett. 583, 1121–1126.

Uhlin, U., Cox, G.B., Guss, J.M., 1997. Crystal structure of the epsilon subunit of the proton-translocating ATP synthase from Escherichia coli. Structure 5, 1219–1230.

Wang, F., Jain, P., Gulten, G., Liu, Z., Feng, Y., Ganesula, K., Motiwala, A.S., Ioerger, T.R., Alland, D., Jacobs, C., Vilchèze Jr., W.R., Sacchettini, J.C., 2010. Mycobacterium tuberculosis dihydrofolate reductase is not a target relevant to the antitubercular activity of isoniazid. Antimicrob. Agents Chemother. 54, 3776–3782.

Waterhouse, A.M., Procter, J.B., Martin, D.M.A., Clamp, M., Barton, G.J., 2009. Jalview Version 2 - a multiple sequence alignment editor and analysis workbench. Bioinformatics 25, 1189–1191.

World Health Organization, 2018. Global tuberculosis report 2018. Available at https://www.who.int/tb/publications/global_report/en/.

Zarco-Zavala, M., Morales-Rios, E., Mendoza-Hernandez, G., Ramirez-Silva, L., Perez-Hernandez, G., Garcia-Trejo, J.J., 2014. The zeta subunit of the F_1F_0-ATP synthase of alpha-proteobacteria controls rotation of the nanomotor with a different structure. FASEB J. 28, 2146–2157.

Zhang, A.T., Montgomery, M.G., Leslie, A.G.W., Cook, G.M., Walker, J.E., 2019. The structure of the catalytic domain of the ATP synthase from Mycobacterium smegmatis is a target for developing antitubercular drugs. 201817615 Proc. Nat. Acad. Sci. USA. https://doi.org/10.1073/pnas.1817615116.

Zharova, T.V., Vinogradov, A.D., 2003. Proton-translocating ATP-synthase of Paracoccus denitrificans: ATP-hydrolytic activity. Biochemistry (Mosc). 68, 1101–1108.